THE JOURNAL OF CELL BIOLOGY

Head-to-tail regulation is critical for the in vivo function of myosin V

Kirk W. Donovan and Anthony Bretscher

Department of Molecular Biology and Genetics, Weill Institute for Cell and Molecular Biology, Cornell University, Ithaca, NY 14853

Cell organization requires regulated cargo transport along cytoskeletal elements. Myosin V motors are among the most conserved organelle motors and have been well characterized in both yeast and mammalian systems. Biochemical data for mammalian myosin V suggest that a head-to-tail autoinhibitory interaction is a primary means of regulation, but the in vivo significance of this interaction has not been studied. Here we generated and characterized mutations in the yeast myosin V Myo2p to reveal that it is regulated by a head-to-tail interaction and that loss of regulation renders the myosin V constitutively active. We show that an unregulated motor is very deleterious for growth, resulting in severe defects in Myo2-mediated transport processes, including secretory vesicle transport, mitochondrial inheritance, and nuclear orientation. All of the defects associated with motor misregulation could be rescued by artificially restoring regulation. Thus, spatial and temporal regulation of myosin V in vivo by a head-to-tail interaction is critical for the normal delivery functions of the motor.

Introduction

The spatial organization of eukaryotic cells depends on a regulated cytoskeleton and motor proteins that use it as tracks for cargo transport and delivery. The major motor proteins implicated in cargo transport are the kinesins and dyneins that use microtubule tracks and unconventional myosins, most notably myosin Vs, which use actin filaments. The delivery cycle of transporting motors must be precisely regulated both spatially and temporally to allow for proper cargo capture and dissociation. Here we examine the in vivo consequences of defects in myosin V motor regulation.

Myosin Vs are highly conserved motor proteins that transport specific cargoes in fungal, plant (called myosin XI), and animal cells (Hammer and Sellers, 2012). In mammalian cells, myosin V motors have been implicated in transporting melanosomes (Wu et al., 1998), recycling endosomes (Lapierre et al., 2001), and the endoplasmic reticulum (Wagner et al., 2011). To perform these functions, all myosin V motors consist of two heavy chains with N-terminal motors dimerizing along a coiled-coil stalk, six associated light chains decorating each force-transducing lever arm, and two cargo-binding globular tail domains at the C terminus (Hammer and Sellers, 2012).

Biochemical and structural data has suggested that mammalian myosin Vs undergo an autoinhibitory interaction between the head domain and globular tail domain. The existence of the folded inhibited state of mammalian myosin V is supported by sedimentation analysis (Krementsov et al., 2004; Li et al., 2004; Wang et al., 2004), cryoelectron microscopy reconstruction (Liu et al., 2006; Thirumurugan et al., 2006), and ATPase activity assays (Li et al., 2008). Activation of the motor occurs after cargo receptor binding for MyoVa in vitro (Li et al., 2005; Sckolnick et al., 2013), as is the case for yeast myosin V in vivo (Donovan and Bretscher, 2012). Notably, the residues predicted to form the ionic bond between domains have been identified (Li et al., 2008; Nascimento et al., 2013). These include mouse MyoVa residues D121/D134/D136 in the head domain and K1706/K1779 in the tail domain. However, despite a decade of work characterizing this interaction biochemically, to our knowledge no one has defined how misregulation of myosin V affects motor functions such as cargo capture and recycling in vivo.

Budding yeast is an especially amenable system in which to probe the function of myosin V motors because of the absence of microtubule-based transport systems (Pruyne et al., 2004). In addition, spatially segregated areas of cargo capture in the mother cell and delivery to the daughter cell enable easy phenotypic analysis. The budding yeast myosin V motor Myo2p is responsible for transporting a wide array of organelles and

Correspondence to Anthony Bretscher: apb5@cornell.edu

Abbreviation used in this paper: FLIP, fluorescence loss in photobleaching.

The Rockefeller University Press $30.00
J. Cell Biol. Vol. 209 No. 3 359–365
www.jcb.org/cgi/doi/10.1083/jcb.201411010

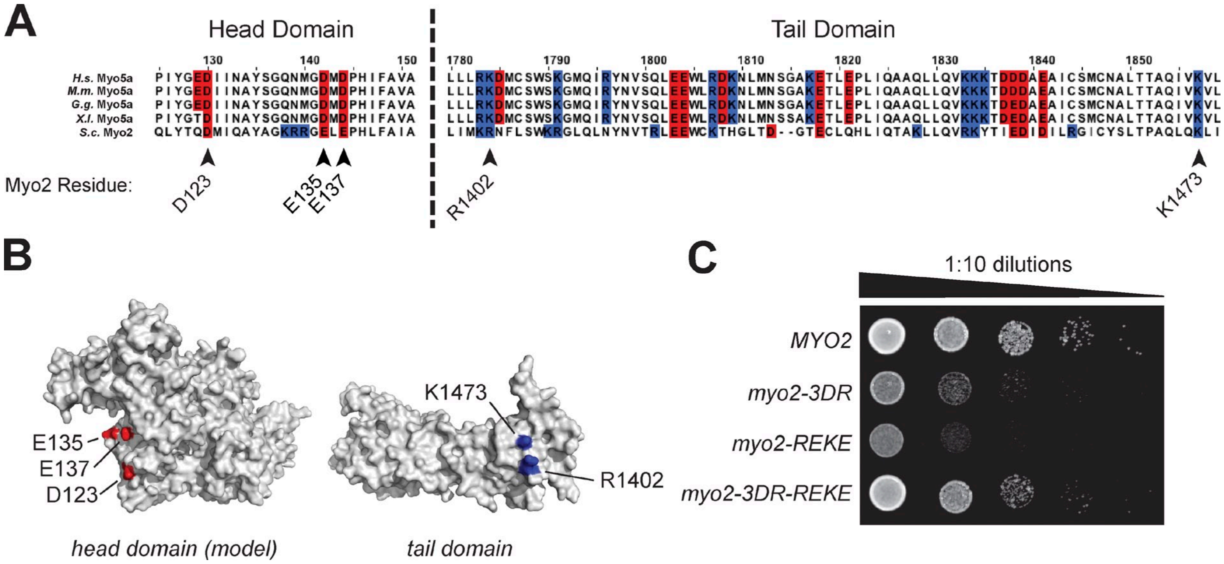

Figure 1. **Charge complementation strongly suggests that Myo2p undergoes a head–tail interaction.** (A) Alignment of myosin V motor protein sequences from vertebrates and budding yeast. Red-shaded letters are acidic residues and blue-shaded letters are basic residues. Numbers atop the alignment show the position along the consensus sequence. Arrowheads point to the three acidic residues and two basic residues proposed to participate in the head–tail interaction, with Myo2p residue number highlighted. *H.s., Homo sapiens*; *M.m., Mus musculus*; *G.g., Gallus gallus*; *X.l., Xenopus laevis*; *S.c., Saccharomyces cerevisiae*. (B) Myo2p head and tail structures displaying the locations of the budding yeast residues from A. Myo2p cargo binding tail (PDB accession no. 2F6H). Head domain structural model was generated from chicken MyoVa head (PDB accession no. 1OE9) as described in Materials and methods. (C) 1:10 serial dilutions of wild-type and charge mutant strains spotted on yeast extract peptone-dextrose and incubated at 30°C for 48 h.

secretory membranes to the daughter cell (Bretscher, 2003). Myo2p also retains the overall domain structure of mammalian myosin V motors, though its coiled-coil rod domain lacks flexible loops and is much shorter than mammalian myosin V.

Here we show that Myo2p is regulated by a head-to-tail interaction and that the length of the lever arm is critical for this interaction. We then document the in vivo consequences of motor misregulation. Defects in this regulatory mechanism lead to a host of cellular problems, including impaired cargo capture and delayed motor recycling.

Results and discussion

We first performed alignment and structural modeling to determine Myo2p's potential to undergo autoinhibition. The five residues predicted to form the ionic bond between the head and tail domains show strong conservation between yeast Myo2p and vertebrate myosin V motors (Fig. 1 A). Although the exact residues may change, the nature of the charges remains the same. These basic tail residues mapped to a patch on the face opposite from the secretory vesicle binding region, whereas the acidic residues in the head were clustered on a modeled Myo2p head in a manner consistent with MyoVa structural studies (Fig. 1 B; Coureux et al., 2003).

As previous attempts to detect a Myo2p head–tail interaction have been unsuccessful (Pashkova et al., 2006), we investigated this interaction by taking a charge complementation approach. The chromosomal *MYO2* gene was mutated such that the basic residues in the interaction were changed to glutamic acid (E) and acidic residues were changed to arginine (R). Mutating the three acidic residues in the head of Myo2p generated the *myo2-3DR* allele (so named because all three residues in mouse MyoVa are aspartic acid), whereas mutating the two basic residues in the tail generated the *myo2-REKE* allele. These two alleles were also combined into the *myo2-3DR-REKE* allele, which effectively swaps the charged patches on the head and tail domains. All mutants expressed similarly to wild type (Fig. S1 A).

The *myo2-3DR* and *myo2-REKE* strains grew much slower than wild-type *MYO2* cells (Fig. 1 C). Note that the strain containing *myo2-REKE* grew slightly slower than *myo2-3DR*; this might be related to the finding that the R1402/K1473 basic patch is also the binding site for exocyst complex component Sec15p, thereby disturbing this nonessential interaction (Fig. S1 B; Jin et al., 2011). To our surprise, the charge-reversal *myo2-3DR-REKE* allele grew nearly as well as wild type, showing that charge complementation between the head and tail is sufficient to return Myo2p to wild-type–like growth. These suppression data, in conjunction with previously published MyoV in vitro work, strongly imply that Myo2p undergoes a head–tail autoinhibitory interaction via these residues (Li et al., 2008).

To determine the effect of the mutant motors in vivo, we first examined their distribution in the cell. We tagged the chromosomal gene encoding Myo2p with a single copy of GFP at its C terminus in wild-type and mutant strains. These tagged strains were functional across a broad range of temperatures and showed no difference in growth compared with the untagged alleles. As expected, Myo2-GFP is polarized toward sites of growth in the daughter cell (Fig. 2 A). However, the bulk of the Myo2-3DR-GFP and Myo2-REKE-GFP motors hyperpolarize toward the bud tip; whole-cell summed projections of medium-budded cells show that 75% of all motors are present in the bud compared with 37% for wild type (Fig. 2 B). Strikingly, when charge reversal mutations in the head and tail were combined

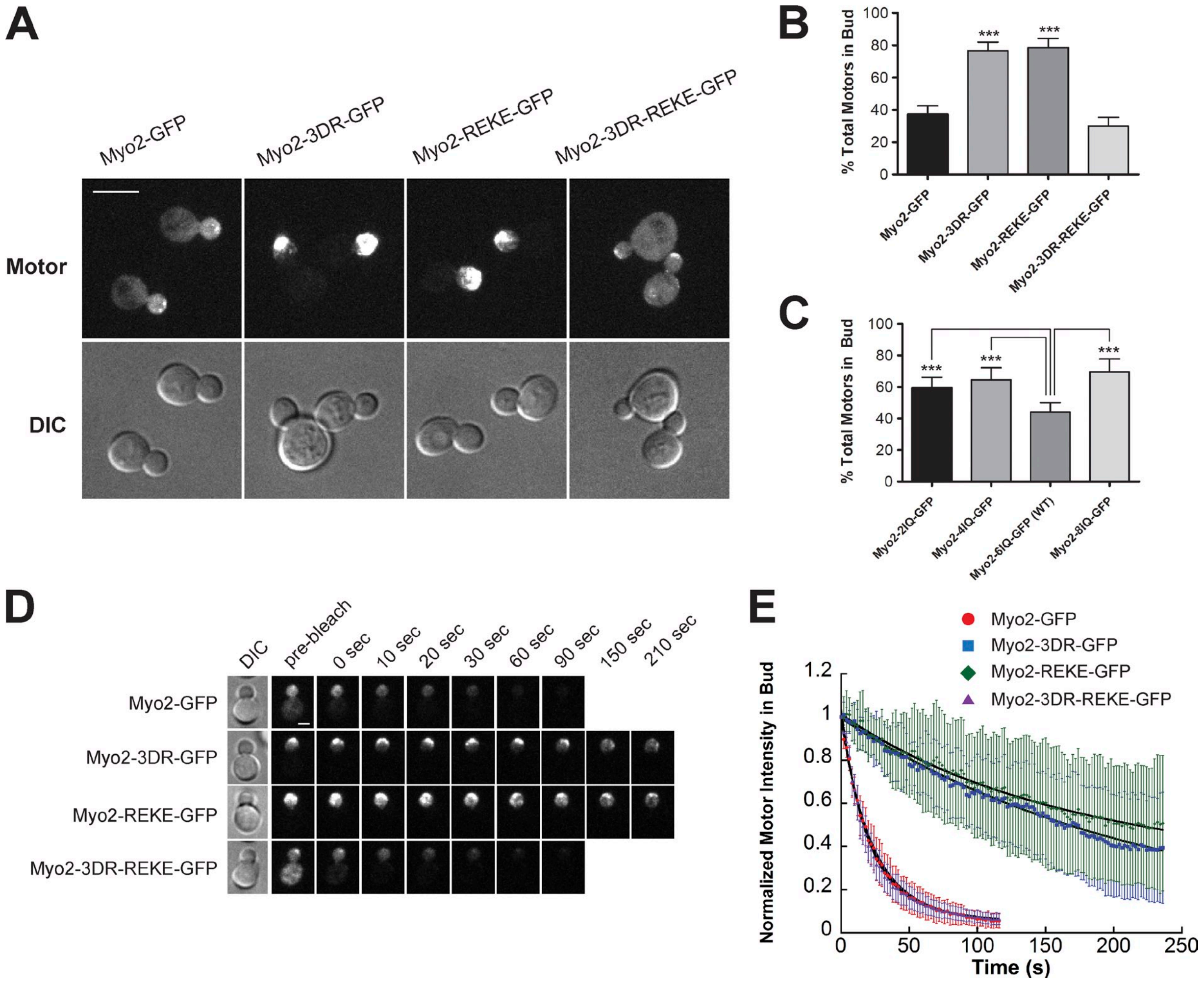

Figure 2. **Inhibiting head–tail regulation causes Myo2p to become hyperpolarized and unable to recycle efficiently.** (A) Maximum projection images of wild-type and charge mutant motors tagged with GFP. Differential interference contrast images shown for clarity. Bar, 5 µm. (B) The percentage of total motors in the bud of wild type and charge mutants, as revealed by whole cell summed projection images. Error bars are the standard deviation for *n* ≥ 40 medium-budded cells per strain. ***, P < 0.0001 versus wild type. (C) The percentage of motors in the bud of wild type and IQ mutants, as revealed by whole cell summed projection images. Error bars are the standard deviation for *n* ≥ 40 medium-budded cells per strain. ***, P < 0.0001 versus wild-type motor-containing 6IQ motifs. (D) Representative still frame micrographs of FLIP experiments for wild-type and charge mutant motors. Mother cells were bleached every 6 s, whereas fluorescence in bud was monitored every 2 s. Differential interference contrast images were used to show outline of the cell. Bar, 2 µm. (E) Graph of the normalized fluorescence intensity in the bud for wild-type and charge mutant motors during FLIP experiments. Error bars are the standard deviation for the indicated strains: Myo2-GFP, *n* = 12; Myo2-3DR-GFP, *n* = 14; Myo2-REKE-GFP, *n* = 12; Myo2-3DR-REKE-GFP, *n* = 15.

in the Myo2-3DR-REKE-GFP strain, the motor phenotype was similar to wild type, with 30% of all motors present in the bud (Fig. 2 B). Therefore, an interaction between the head and tail domains is necessary and sufficient to regulate myosin V in vivo to achieve a normal distribution.

The two internal loops present in mammalian myosin V coiled-coil stalks have been shown in vitro to be required for autoinhibition, likely because of the flexibility gained to bring the head and tail domains together (Li et al., 2006). Myo2p lacks these internal loops, though the length of the lever arm and coiled coil domains are nearly identical (∼21 and 24 nm, respectively). We therefore explored the effect of disturbing this geometry by subtracting or adding light-chain binding IQ motifs, thereby shortening or lengthening its lever arm (Schott et al., 2002). Motors with 2, 4, or 8 IQ motifs on the lever arm showed significantly more motors in the bud compared with wild-type 6IQ motors (Fig. 2 C). Thus, the absolute length of the lever arm is important for proper motor regulation in vivo, with mismatched lengths resulting in more motors in the active state.

Next, we explored in detail how the motor delivery cycle is perturbed in the Myo2p charge mutants. A myosin V motor must be deactivated for efficient recycling from sites of delivery, and this occurs when it releases its cargo (Donovan and Bretscher, 2012). To determine if the head–tail interaction is necessary to deactivate the motor and allow normal recycling, we performed fluorescence loss in photobleaching (FLIP) experiments. Motors in the mother cell were bleached every 6 s, whereas the intensity of motor fluorescence in the bud was monitored every 2 s. Wild-type motors followed known recycling kinetics, with the vast majority of motors leaving the bud after ∼30 s (Fig. 2, D and E; Donovan and Bretscher, 2012). Myo2-3DR-GFP or Myo2-REKE-GFP motors resided in the bud for much longer, with half-times of loss being ∼2–3 min. This suggests that motors unable to form the head–tail interaction are

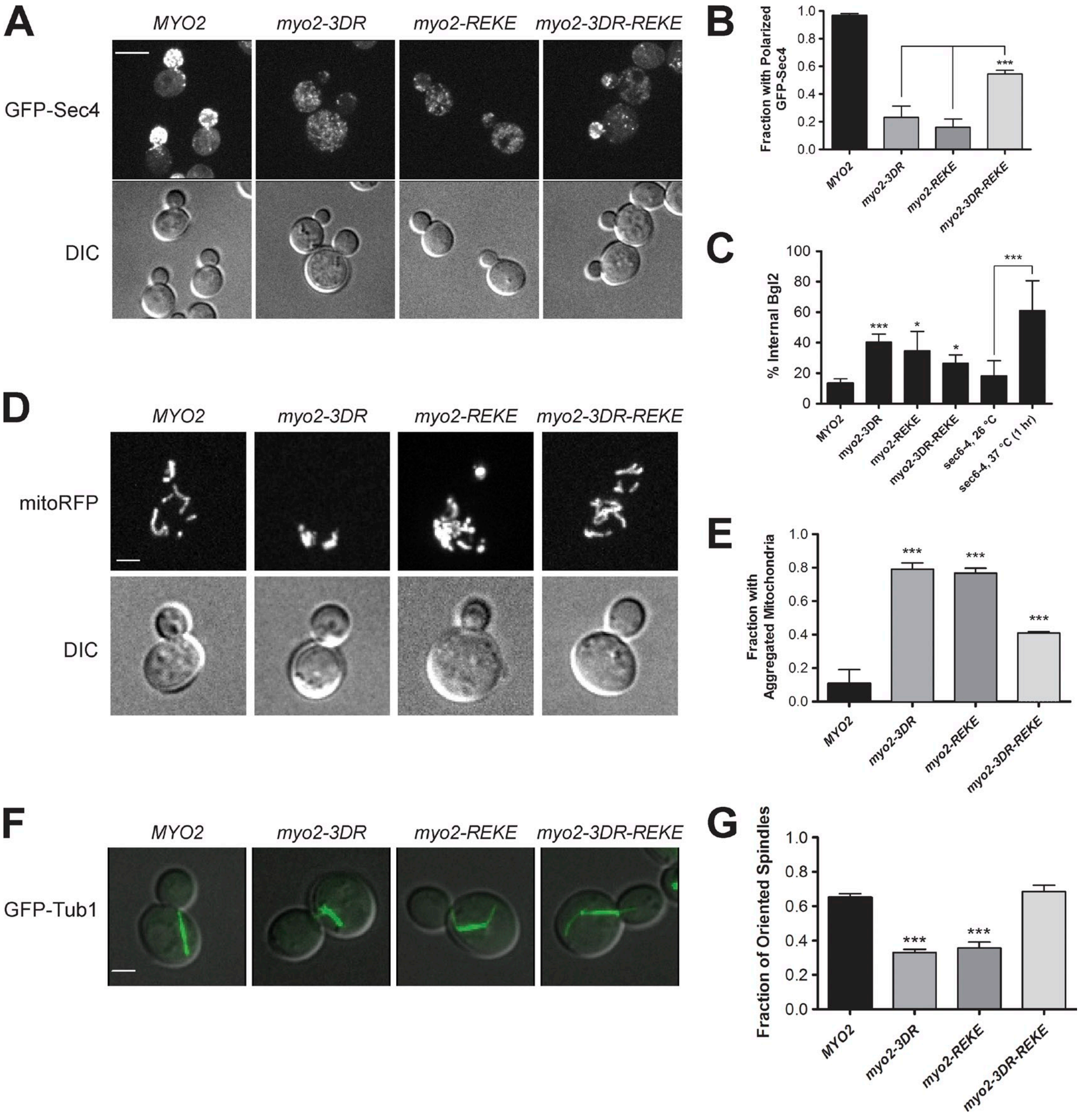

Figure 3. **Cargo transport functions of an unregulated myosin V are severely compromised.** (A) Maximum projection images of GFP-Sec4 in wild-type and charge mutant strains. Differential interference contrast images shown for clarity. Bar, 5 µm. (B) Fraction of cells with polarized GFP-Sec4 vesicles. 100+ medium budded cells were scored for each strain; *n* = 3 replicates. ***, P < 0.0001. (C) Percentage of Bgl2p found in the internal fraction of wild-type, *sec6-4*, and charge mutant strains; *n* = 4 replicates. *, P < 0.05; ***, P < 0.0001. (D) Maximum projection images of mitochondrial RFP marker in wild-type and charge mutant strains. Differential interference contrast images shown for clarity, and contrast was adjusted for best presentation. Bar, 2 µm. (E) Fraction of cells with aggregated mitochondria in mother cell. 100+ medium budded cells were scored for each strain; *n* = 3 replicates. ***, P < 0.0001 versus wild type. (F) Maximum projection images of GFP-Tub1 in wild-type and charge mutant strains. Bar, 2 µm. (G) Fraction of cells with oriented spindles, as defined by the axis of the spindle passing through the bud neck. 100+ medium budded cells were scored for each strain; *n* = 3 replicates. ***, P < 0.0001 versus wild type. Error bars are the standard deviation.

hyperactive and unable to recycle. Strikingly, in the charge complementation Myo2-3DR-REKE-GFP allele, motors recycled at rates matching wild-type motors. Thus, the head–tail autoinhibitory interaction is required for proper recycling dynamics of myosin V.

What effect does misregulation of the autoinhibitory interaction have on cargo transport? Myo2p has two known essential cargoes: mitochondria, where Mmr1p and the Rab Ypt11p serve as alternative receptors, and secretory vesicles, where the Rab Sec4p and an unknown component dependent on the lipid PI4P serve as receptors (Itoh et al., 2002, 2004; Santiago-Tirado et al., 2011; Jin et al., 2011; Chernyakov et al., 2013). Importantly, these cargoes bind to different locations on the tail (Pashkova et al., 2006; Eves et al., 2012); Mmr1p binds to subdomain I, whereas the Rabs Sec4p/Ypt11p bind to subdomain II (and on the face opposite Mmr1p binding).

Wild-type cells show very robust polarization of the secretory vesicle marker GFP-Sec4 (Fig. 3, A and B). In contrast, in both charge mutant alleles there is a large buildup of GFP-Sec4–marked vesicles in the mother cell and a large decrease in the fraction of cells with polarized GFP-Sec4 (Fig. 3 B). This does not appear to be a defect in Sec15p binding, an interaction also using the R1402/K1473 basic patch (Jin et al., 2011), because the result is phenocopied in the *myo2-3DR* strain.

Because both Myo2-3DR and Myo2-REKE motors are constitutively active and accumulate at the bud tip, it is likely that the defect in vesicle transport is caused by a scarcity of available motors in the mother cell. In the charge reversal *myo2-3DR-REKE* strain, GFP-Sec4 polarization is significantly restored, though not to quite to the same degree as seen in wild-type cells. Exocyst component Sec15-GFP was also polarized in the *myo2-3DR-REKE* allele (Fig. S1 C), suggesting that defects in polarized transport related to this site may not be completely caused by a compromised Sec15p–Myo2p interaction as has been previously reported (Jin et al., 2011), but instead caused by motor misregulation.

To explore if the failure of the unregulated mutants to transport secretory vesicles affected exocytosis of secretory vesicle cargo, we examined the internal pool of the β-endoglucanase Bgl2p, a marker for post-Golgi secretory vesicles (Harsay and Bretscher, 1995). As a benchmark, the conditional exocyst mutant *sec6-4* accumulates substantial Bgl2p after a 1-h shift to the restrictive temperature (Fig. 3 C). 13% of the total Bgl2p population is present inside wild-type cells, which increases >2.5-fold in each Myo2p charge mutant (Fig. 3 C). The charge reversal *myo2-3DR-REKE* mutant also exhibited significantly increased Bgl2p accumulation; this could be a result of slight defects in vesicle fusion because the Sec15p interaction through R1402/K1473 is compromised (Fig. S1 B).

We next turned to see how mitochondria are distributed in the cell. In wild-type cells, mitochondria appear as a tubulated network in both the mother and bud as visualized with a mito-RFP probe (Fig. 3 D). In either of the *myo2-3DR* or *myo2-REKE* strains, mitochondria adopted a less tubular and aggregated appearance toward the back of the mother cell. This phenotype is also observed in cells that have an impaired ability to transport mitochondria into the bud (Chernyakov et al., 2013; Klecker et al., 2013). When both mutations were combined, there was a significant decrease in the fraction of cells with this phenotype and a majority of cells had a normal mitochondrial distribution and appearance (Fig. 3 E).

We also examined the orientation of the mitotic spindle, a process in which the receptor Kar9p binds to subdomain II of the Myo2p tail to link the motor to the end of a microtubule via Bim1p (Yin et al., 2000; Eves et al., 2012). Single-charge *myo2* mutants had significantly fewer cells displaying oriented spindles, as scored by the spindle axis passing directly through the bud neck. Complementing charges in the *myo2-3DR-REKE* mutant fully restored orientation to wild-type levels (Fig. 3, F and G). Thus, misregulation of autoinhibition compromises the ability of Myo2 to orient the mitotic spindle.

The similar deleterious effects of the charge mutants and their suppression in the charge reversal mutant, for secretory vesicle polarization, mitochondrial distribution, and spindle orientation, are important because the cargo receptors bind to different regions of the Myo2p tail. Thus, it is unlikely that such large-scale cellular changes are caused by defects in binding cargo, but are instead caused by motor misregulation. Therefore, motor misregulation in vivo leads to severe cargo transport defects.

The data presented here indicate that a head-to-tail inhibitory interaction regulates yeast Myo2p as it does mammalian Myosin Va. More importantly, our results provide the first direct evidence that misregulation of a myosin V motor in vivo leads to wide-ranging cellular problems, including reduced abilities to capture and transport cargo as well as recycle after cargo delivery. Because the bulk of misregulated motors are hyperpolarized to sites of growth and kinetically delayed in recycling, the pool of motors available to allow continuous cargo transport is insufficient. Thus, myosin V motors have evolved and conserved the ability to remain firmly inactive until cargo is available, transport it in a processive manner, and finally coordinate delivery with motor deactivation.

Materials and methods

Yeast strains and molecular biology techniques

Cells were grown and selected for using standard molecular biology techniques. Yeast transformations were performed using lithium acetate–based methods (Gietz et al., 1995). In brief, log phase 5-ml cultures were transformed for 45 min at 42°C with the plasmid/PCR product in a mixture containing ~40% wt/vol PEG-3350 (Sigma-Aldrich), 0.1 M lithium acetate (Sigma-Aldrich), and 0.28 mg/ml SS carrier DNA (Sigma-Aldrich). Dilution assays were spotted on appropriate media by 1:10 serial dilutions and incubated at the indicated temperature.

Homology and structural work

Protein sequences of myosin V motors were obtained from the Uniprot database (accession nos. Q9Y4I1, Q99104, Q02440, K4JEU1, and P19524) and aligned with JalView software (Waterhouse et al., 2009) using the TCoffeeWS algorithm. The location of the basic patch on the Myo2p tail was found using the Myo2p tail crystal structure (PDB accession no. 2F6H; Pashkova et al., 2006). A structural model of the Myo2p head domain was constructed by threading the primary sequence (residues 1–785) of the Myo2p head domain around a chicken MyoVa head structure (PDB accession no. 1OE9; Coureux et al., 2003) using the SWISS-MODEL server (University of Basel, Basel, Switzerland).

DNA constructs

To generate the *myo2-3DR* mutant, constructs were created to mutate residues D123/E135/E137 to arginine and integrate them into the endogenous *MYO2* locus. The region −500 to +750 (containing the promoter and the first 750 nucleotides of *MYO2*) was amplified from genomic DNA of a wild-type BY4741 strain with XhoI and BamHI sites at the end of the forward and reverse primers, respectively, using the Expand High Fidelity PCR kit (Roche). After overnight digestion, this was then ligated into a similarly cut pRS303 vector. A second homology region containing nucleotides −968 to −500 was amplified and ligated between the BamHI and NotI sites of the vector. To mutate residues in the head proposed to be involved in the interaction to arginine, the QuikChange II XL kit (Agilent Technologies) was used with primers designed to introduce the appropriate mutations. Sequencing was performed on all amplified products as well as after site-directed mutagenesis to ensure fidelity. After digestion of the unique BamHI site in the vector, the vectors containing the mutations were transformed into cells and selected for using SD-His media. Sequencing genomic DNA of the resulting colonies ensured the mutations were present at the *myo2* locus.

A similar strategy was used to mutate the R1402/K1473 residues in the tail to glutamic acid, using the pRS303-Myo2tail-3′UTR integrating vector as a template (Schott et al., 1999). This base vector contains nucleotides 3272–4725 (those after an internal SpeI restriction site in the tail domain) along with a 197-nucleotide fragment of the 3′UTR; digesting with SpeI will linearize the vector and allow for integration of any introduced mutations into the endogenous *MYO2* gene. To generate the *myo2-3DR-REKE* strain, this plasmid with associated *REKE* mutations was swapped into the pRS305 vector (*LEU2* marker) to allow for its selection when transformed into *myo2-3DR::HIS3*. Wild-type and mutant expression levels were performed via glass-bead disruption methods and probed with a Myo2p tail polyclonal antibody (Schott et al., 1999; generated in rabbit against the Myo2p tail domain).

Motors were observed by appending GFP to the C terminus using a pRS306-cctail-GFP construct as previously described (Donovan and Bretscher, 2012). This construct contains the cctail region of *MYO2* (nucleotides 2776–4725) fused to one copy of GFP at the C terminus, followed by the *MYO2* terminator. When digested with the internal unique HindIII site, the vector integrates into the endogenous *MYO2* locus. The appropriate mutations from the *myo2-REKE* allele were transferred into this construct before integration to ensure the mutations were not selected against. Sequencing of genomic DNA was performed to ensure the mutations remained.

Microscopy

Live cell imaging of log-phase cells was performed at room temperature (21°C) on a CSU-X spinning disc confocal microscope system (Intelligent Imaging Innovations) using an inverted microscope (DMI600B; Leica), 100×/1.46 NA objective, and either the CoolSnap HQ2 camera (Photometrics) or QuantEM EMCCD camera (Photometrics). Strains were imaged on a 2% agarose pad with synthetic complete media. For longer time-lapse experiments with photobleaching, a 35-mm dish pretreated with 0.05 mg/ml concanavalin A (EY Laboratories) to adhere the cells was used. Micrographs were acquired in Slidebook (Intelligent Imaging Innovations), which was also used to create maximum image projections for single images.

The percentage of motors in the bud was calculated in ImageJ using the integrated density of summed projections of the mother cell and bud, after subtracting out the background; only cells with medium-sized buds (2-µm diameter) were used in the analysis. FLIP experiments were performed such that a 3-µm z-stack of the cell (which included all of the medium-sized buds) was imaged every 2 s, with mother-cell bleach events occurring every 6 s. Bleaching was performed using the Vector control system (Intelligent Imaging Innovations) with 1-ms dwell times and laser power set to 60%. Analysis of FLIP photobleaching was also performed in Slidebook software, where the motor intensity in the bud of summed movie projections over time was calculated (after subtracting background and using an adjacent unbleached control cell for normalization).

Cargo phenotypes in charge mutants were observed and scored by transforming the appropriate cargo marker. Secretory vesicles were imaged using the endogenously integrated GFP-Sec4 marker (Donovan and Bretscher, 2012), which contains 400 nucleotides of the *SEC4* promoter, *GFP*, *SEC4*, and the *SEC4* terminator. Cells were scored as having polarized or not polarized secretory vesicles. Mitochondria were observed by transforming in the pRS306-mitoRFPff-ura3d integrating vector (Chernyakov et al., 2013) and scored as either having aggregated mitochondria or normal mitochondria in the mother cell. Spindle orientation was observed using a GFP-Tub1 construct (pAFS125-GFP-Tub1, containing the *HIS3* promoter, *GFP*, and *TUB1* locus and terminator) integrated into the *TUB1* locus (Yin et al., 2000). Cells were scored as either oriented (with the spindle axis passing through the bud neck) or not oriented. Sec15-GFP::kanMX6 polarization was detected by C-terminal integration of a PCR cassette into the chromosomal *SEC15* locus (Longtine et al., 1998).

Bgl2 assay

To probe for secretion defects, the fraction of internal β-endoglucanase Bgl2p was determined by separating internal and external fractions. Cells were grown in 5 ml of yeast extract peptone-dextrose at 26°C to log phase. A control strain, *sec6-4*, was transferred to 37°C for 1 h. Cells were then killed in killing buffer (10 mM NaF/10 mM NaN_3 in 10 mM Tris, pH 7.4) and washed on ice in buffer B (1.2 M sorbitol, 25 mM K-P_i, and 25 mM BME, pH 7.4) containing killing buffer. Cells were spheroplasted to remove the cell wall with 100 µl of 25 µM Zymolyase 100T in buffer B at 37°C for 1 h. After a low speed spin at 500 *g*, the supernatant containing the external fraction was gently harvested from the pellet containing the internal fraction. The pellet was resuspended in an equal volume of 10 mM MOPS buffer as the supernatant, and then both fractions were boiled after addition of Laemmli sample buffer. Fractions of all strains were run out on SDS-PAGE gels, transferred by semi-dry methods, and probed using a rabbit-derived anti-Bgl2p antibody serum. The internal fraction was found by dividing the internal fraction by the total amount of Bgl2p in both fractions.

Statistics

Student's *t* test and one-way analysis of variance were used to determine statistical significance between measured values. A 95% confidence interval ($P < 0.05$) was accepted as significant.

Online supplemental material

Fig. S1 provides data showing charge mutant strains are expressed similarly to wild type and affect Sec15p binding and localization as expected. A list of strains used in this study is also included in Table S1. Online supplemental material is available at http://www.jcb.org/cgi/content/full/jcb.201411010/DC1.

We thank L. Xu for initial construction of the head domain vector and other members of the Bretscher Laboratory for their comments and suggestions during the course of this work.

This work was funded by Public Health Service grant GM39066 to A. Bretscher.

The authors declare no competing financial interests.

Submitted: 4 November 2014
Accepted: 2 April 2015

References

Bretscher, A. 2003. Polarized growth and organelle segregation in yeast: the tracks, motors, and receptors. *J. Cell Biol.* 160:811–816. http://dx.doi.org/10.1083/jcb.200301035

Chernyakov, I., F. Santiago-Tirado, and A. Bretscher. 2013. Active segregation of yeast mitochondria by Myo2 is essential and mediated by Mmr1 and Ypt11. *Curr. Biol.* 23:1818–1824. http://dx.doi.org/10.1016/j.cub.2013.07.053

Coureux, P.-D., A.L. Wells, J. Ménétrey, C.M. Yengo, C.A. Morris, H.L. Sweeney, and A. Houdusse. 2003. A structural state of the myosin V motor without bound nucleotide. *Nature*. 425:419–423. http://dx.doi.org/10.1038/nature01927

Donovan, K.W., and A. Bretscher. 2012. Myosin-V is activated by binding secretory cargo and released in coordination with Rab/exocyst function. *Dev. Cell*. 23:769–781. http://dx.doi.org/10.1016/j.devcel.2012.09.001

Eves, P.T., Y. Jin, M. Brunner, and L.S. Weisman. 2012. Overlap of cargo binding sites on myosin V coordinates the inheritance of diverse cargoes. *J. Cell Biol.* 198:69–85. http://dx.doi.org/10.1083/jcb.201201024

Gietz, R.D., R.H. Schiestl, A.R. Willems, and R.A. Woods. 1995. Studies on the transformation of intact yeast cells by the LiAc/SS-DNA/PEG procedure. *Yeast*. 11:355–360. http://dx.doi.org/10.1002/yea.320110408

Hammer, J.A. III, and J.R. Sellers. 2012. Walking to work: roles for class V myosins as cargo transporters. *Nat. Rev. Mol. Cell Biol.* 13:13–26.

Harsay, E., and A. Bretscher. 1995. Parallel secretory pathways to the cell surface in yeast. *J. Cell Biol.* 131:297–310. http://dx.doi.org/10.1083/jcb.131.2.297

Itoh, T., A. Watabe, A. Toh-E, and Y. Matsui. 2002. Complex formation with Ypt11p, a rab-type small GTPase, is essential to facilitate the function of Myo2p, a class V myosin, in mitochondrial distribution in *Saccharomyces cerevisiae*. *Mol. Cell. Biol.* 22:7744–7757. http://dx.doi.org/10.1128/MCB.22.22.7744-7757.2002

Itoh, T., A. Toh-E, and Y. Matsui. 2004. Mmr1p is a mitochondrial factor for Myo2p-dependent inheritance of mitochondria in the budding yeast. *EMBO J.* 23:2520–2530. http://dx.doi.org/10.1038/sj.emboj.7600271

Jin, Y., A. Sultana, P. Gandhi, E. Franklin, S. Hamamoto, A.R. Khan, M. Munson, R. Schekman, and L.S. Weisman. 2011. Myosin V transports secretory vesicles via a Rab GTPase cascade and interaction with the exocyst complex. *Dev. Cell*. 21:1156–1170. http://dx.doi.org/10.1016/j.devcel.2011.10.009

Klecker, T., D. Scholz, J. Förtsch, and B. Westermann. 2013. The yeast cell cortical protein Num1 integrates mitochondrial dynamics into cellular architecture. *J. Cell Sci.* 126:2924–2930. http://dx.doi.org/10.1242/jcs.126045

Krementsov, D.N., E.B. Krementsova, and K.M. Trybus. 2004. Myosin V: regulation by calcium, calmodulin, and the tail domain. *J. Cell Biol.* 164:877–886. http://dx.doi.org/10.1083/jcb.200310065

Lapierre, L.A., R. Kumar, C.M. Hales, J. Navarre, S.G. Bhartur, J.O. Burnette, D.W. Provance Jr., J.A. Mercer, M. Bähler, and J.R. Goldenring. 2001. Myosin Vb is associated with plasma membrane recycling systems. *Mol. Biol. Cell*. 12:1843–1857. http://dx.doi.org/10.1091/mbc.12.6.1843

Li, X.-D., K. Mabuchi, R. Ikebe, and M. Ikebe. 2004. Ca^{2+}-induced activation of ATPase activity of myosin Va is accompanied with a large conformational change. *Biochem. Biophys. Res. Commun.* 315:538–545. http://dx.doi.org/10.1016/j.bbrc.2004.01.084

Li, X.-D., R. Ikebe, and M. Ikebe. 2005. Activation of myosin Va function by melanophilin, a specific docking partner of myosin Va. *J. Biol. Chem.* 280:17815–17822. http://dx.doi.org/10.1074/jbc.M413295200

Li, X.-D., H.S. Jung, K. Mabuchi, R. Craig, and M. Ikebe. 2006. The globular tail domain of myosin Va functions as an inhibitor of the myosin Va motor. *J. Biol. Chem.* 281:21789–21798. http://dx.doi.org/10.1074/jbc.M602957200

Li, X.-D., H.S. Jung, Q. Wang, R. Ikebe, R. Craig, and M. Ikebe. 2008. The globular tail domain puts on the brake to stop the ATPase cycle of myosin Va. *Proc. Natl. Acad. Sci. USA*. 105:1140–1145. http://dx.doi.org/10.1073/pnas.0709741105

Liu, J., D.W. Taylor, E.B. Krementsova, K.M. Trybus, and K.A. Taylor. 2006. Three-dimensional structure of the myosin V inhibited state by cryoelectron tomography. *Nature*. 442:208–211.

Longtine, M.S., A. McKenzie III, D.J. Demarini, N.G. Shah, A. Wach, A. Brachat, P. Philippsen, and J.R. Pringle. 1998. Additional modules for versatile and economical PCR-based gene deletion and modification in *Saccharomyces cerevisiae*. *Yeast*. 14:953–961. http://dx.doi.org/10.1002/(SICI)1097-0061(199807)14:10<953::AID-YEA293>3.0.CO;2-U

Nascimento, A.F.Z., D.M. Trindade, C.C.C. Tonoli, P.O. de Giuseppe, L.H.P. Assis, R.V. Honorato, P.S.L. de Oliveira, P. Mahajan, N.A. Burgess-Brown, F. von Delft, et al. 2013. Structural insights into functional overlapping and differentiation among myosin V motors. *J. Biol. Chem.* 288:34131–34145. http://dx.doi.org/10.1074/jbc.M113.507202

Pashkova, N., Y. Jin, S. Ramaswamy, and L.S. Weisman. 2006. Structural basis for myosin V discrimination between distinct cargoes. *EMBO J.* 25:693–700. http://dx.doi.org/10.1038/sj.emboj.7600965

Pruyne, D., A. Legesse-Miller, L. Gao, Y. Dong, and A. Bretscher. 2004. Mechanisms of polarized growth and organelle segregation in yeast. *Annu. Rev. Cell Dev. Biol.* 20:559–591. http://dx.doi.org/10.1146/annurev.cellbio.20.010403.103108

Santiago-Tirado, F.H., A. Legesse-Miller, D. Schott, and A. Bretscher. 2011. PI4P and Rab inputs collaborate in myosin-V-dependent transport of secretory compartments in yeast. *Dev. Cell*. 20:47–59. http://dx.doi.org/10.1016/j.devcel.2010.11.006

Schott, D., J. Ho, D. Pruyne, and A. Bretscher. 1999. The COOH-terminal domain of Myo2p, a yeast myosin V, has a direct role in secretory vesicle targeting. *J. Cell Biol.* 147:791–808. http://dx.doi.org/10.1083/jcb.147.4.791

Schott, D.H., R.N. Collins, and A. Bretscher. 2002. Secretory vesicle transport velocity in living cells depends on the myosin-V lever arm length. *J. Cell Biol.* 156:35–39. http://dx.doi.org/10.1083/jcb.200110086

Sckolnick, M., E.B. Krementsova, D.M. Warshaw, and K.M. Trybus. 2013. More than just a cargo adapter, melanophilin prolongs and slows processive runs of myosin Va. *J. Biol. Chem.* 288:29313–29322. http://dx.doi.org/10.1074/jbc.M113.476929

Thirumurugan, K., T. Sakamoto, J.A. Hammer III, J.R. Sellers, and P.J. Knight. 2006. The cargo-binding domain regulates structure and activity of myosin 5. *Nature*. 442:212–215. http://dx.doi.org/10.1038/nature04865

Wagner, W., S.D. Brenowitz, and J.A. Hammer III. 2011. Myosin-Va transports the endoplasmic reticulum into the dendritic spines of Purkinje neurons. *Nat. Cell Biol.* 13:40–48. http://dx.doi.org/10.1038/ncb2132

Wang, F., K. Thirumurugan, W.F. Stafford, J.A. Hammer III, P.J. Knight, and J.R. Sellers. 2004. Regulated conformation of myosin V. *J. Biol. Chem.* 279:2333–2336. http://dx.doi.org/10.1074/jbc.C300488200

Waterhouse, A.M., J.B. Procter, D.M.A. Martin, M. Clamp, and G.J. Barton. 2009. Jalview Version 2—a multiple sequence alignment editor and analysis workbench. *Bioinformatics*. 25:1189–1191. http://dx.doi.org/10.1093/bioinformatics/btp033

Wu, X., B. Bowers, K. Rao, Q. Wei, and Hammer JA III. 1998. Visualization of melanosome dynamics within wild-type and dilute melanocytes suggests a paradigm for myosin V function in vivo. *J. Cell Biol.* 143:1899–1918. http://dx.doi.org/10.1083/jcb.143.7.1899

Yin, H., D. Pruyne, T.C. Huffaker, and A. Bretscher. 2000. Myosin V orientates the mitotic spindle in yeast. *Nature*. 406:1013–1015. http://dx.doi.org/10.1038/35023024